PAPER • **OPEN ACCESS**

Development of a GEM based diagnostic for soft x-ray measurements resolved in space, time, and energy at RFX-mod2

To cite this article: F Guiotto *et al* 2025 *Plasma Phys. Control. Fusion* **67** 125013

OPEN ACCESS
IOP Publishing
Plasma Physics and Controlled Fusion
Plasma Phys. Control. Fusion **67** (2025) 125013 (17pp)
https://doi.org/10.1088/1361-6587/ae26c6

Development of a GEM based diagnostic for soft x-ray measurements resolved in space, time, and energy at RFX-mod2

F Guiotto[2,4,5,*], O Putignano[2], A Dal Molin[2], G Croci[1,2,3], P Franz[4], M Zuin[4], L Orlandi[4,5], A Celora[1,2], F Caruggi[1,2], G Grosso[2], E Perelli Cippo[2], M Tardocchi[2], P Bettini[4,5,6] and A Muraro[2]

[1] Dipartimento di Fisica 'G. Occhialini', Università di Milano-Bicocca, Piazza della Scienza 3, Milano, Italy
[2] Istituto per la Scienza e Tecnologia dei Plasmi, Consiglio Nazionale delle Ricerche, Via Roberto Cozzi 53, Milano, Italy
[3] INFN, Sezione Milano-Bicocca, Piazza della Scienza 3, Milano 20125, Italy
[4] Consorzio RFX (CNR, ENEA, INFN, Università di Padova, Acciaierie Venete), Corso Stati Uniti 4, Padova, Italy
[5] Centro Ricerche Fusione (CRF)—University of Padova, C.so Stati Uniti 4, 35127 Padova, Italy
[6] Dipartimento di Ingegneria Industriale—DII, Università di Padova, Via G. Gradenigo 6/A, Padova, Italy

E-mail: federico.guiotto@phd.unipd.it

Received 7 August 2025, revised 25 November 2025
Accepted for publication 2 December 2025
Published 19 December 2025

Abstract

This study presents the development of an advanced soft x-ray (SXR) diagnostic for the RFX-mod2 device, tailored for photon energies of ∼1–25 keV. The system will consist of two gas electron multiplier (GEM) detectors designed to enable energy-resolved 1D tomographic reconstructions (i.e. reconstructions of the SXR radial emissivity profiles). Simulations have shown its potential to achieve a spatial resolution of ∼1 cm and to differentiate between thermal and suprathermal plasma components. This capability is particularly valuable for RFX-mod2, where strong magnetic reconnection events are expected to generate significant SXR spectral tails in localized regions. The GEM-based diagnostic will therefore complement the SXR silicon photodiode arrays (SiPh) foreseen for installation at RFX-mod2 [2]. SiPh have been successfully employed for two-dimensional tomographic reconstruction of the SXR emissivity at RFX-mod. However, their operation in current mode allows only measurements of photon flux, lacking energy resolution. In contrast, GEM detectors operate in photon-counting mode. They provide energy-resolved measurements with a temporal resolution of ∼10 μs and an energy resolution of ∼20% at 6 keV. They also offer a high rate capability (∼1 MHz/channel) and high radiation hardness. This paper presents the CAD model of the GEM diagnostic, as well as the custom-made simulations used to drive design choices and develop the energy resolved 1D tomographic reconstruction algorithm.

* Author to whom any correspondence should be addressed.

Keywords: magnetic confinement fusion, RFX-mod2, gas electron multiplier detectors, diagnostic design, x-ray spectroscopy, tomographic reconstruction resolved in energy

1. Introduction

1.1. RFX-mod2 and gas electron multiplier (GEM) detectors

The reversed-field pinch (RFP) configuration [1]—employed in devices such as RFX-mod2 [2] in Padua and MST [3] in Madison—has been a rich environment for studying the role of magnetic reconnection in suprathermal particle acceleration. In these plasmas, several tearing modes can nonlinearly couple and release large amounts of magnetic energy during sawtooth-like relaxation events, generating suprathermal electron populations that in turns lead to distinctive high-energy tails in the soft x-ray (SXR) emission. An example can be found in [4], for the MST experiment, where SXR spectral tails in the 10–30 keV range were observed. Such findings highlight the importance of deploying diagnostics capable of simultaneously measuring the position, time, and energy of incident photons, in order to discriminate the thermal component from the higher-energy suprathermal tail in the SXR emission.

Electron acceleration related to magnetic reconnection has been observed not only in RFP devices, but also in tokamaks such as MAST-U [5], and EAST [6].

In the past, SXR measurements in the RFX-mod device have relied on silicon photodiodes [7] operated in current mode for tomographic reconstructions and electron temperature (T_e) determinations through the double filter technique [8]. These diagnostics have yielded robust flux data, but provided no energy discrimination. As the RFX-mod2 upgrade pursues improved diagnostic capabilities and explores novel regimes—potentially featuring stronger magnetic reconnection and more pronounced suprathermal electron populations—an energy-resolved, high-rate SXR diagnostic becomes of great importance. Possible energization of electrons is anticipated to be transient on a $\sim$10 μs time scale, making high time resolution measurements necessary to reveal electron dynamics.

GEM technology [9] addresses these needs effectively. Designed for photon-counting operation, GEM detectors offer a high rate capability ($\sim$1 MHz/channel) high temporal resolution ($\sim$10 μs) and moderate energy resolution ($\sim$20% at 6 keV) [10]. GEM detectors have already been employed in different nuclear fusion devices, such as JET [11], MAST-U [5], WEST [12], KSTAR [13], and EAST [6, 14]. In particular, at MAST-U and EAST, they have been used to observe macroscopic plasma instabilities and magnetic reconnection events [5, 6].

GEM detectors are also foreseen for installation in future devices, such as DTT [15] and DEMO [16].

In this work, we present the development of an advanced GEM-based SXR diagnostic (consisting of two separate GEM detectors) for the RFX-mod2 device, covering energies from 1 to 25 keV. The configuration for SXR detection described in this work is the triple-GEM detector, made up of three GEM foils coated with aluminum or copper. The photoelectric interaction of the impinging photons and the first gas ionization occur in the drift zone between the cathode (which consists of a thin aluminized Mylar window) and the first GEM foil. The number of electron-ion pairs generated is proportional to the energy of the incoming radiation [17]. The primary electrons, carried by the electric field, drift towards the GEM foils, traverse the holes, and are multiplied in each of the three stages of the cascade. In the final induction region they are carried to a pixelated anode, made of several gold-coated copper pads, producing a detectable signal for each original incoming photon. For each photon detected by a given pixel, two quantities are recorded: the time of arrival and the time-over-threshold (TOT). The TOT represents the duration for which the signal remains above the discrimination threshold and is related to the energy deposited by the photon. Through an appropriate calibration curve, as described in [10], the TOT values can be converted into corresponding energy values, enabling energy-resolved measurements.

The voltage difference on each GEM foil is set independently with a custom designed High Voltage module called HVGEM [10, 18]. A diagram representing a triple-GEM detector is shown in figure 1.

Through simulations based on past RFX-mod data and the current GEM diagnostic design, in this work we evaluate its ability to reconstruct emissivity profiles with $\sim$1 cm spatial resolution and to distinguish between thermal and suprathermal SXR components.

1.2. REVOLT-U software

Designing advanced SXR detectors—such as GEMs—for fusion devices requires a simulation tool that balances accuracy, speed, and computational efficiency. While Monte Carlo frameworks (like MCNP [19] and GEANT4 [20]) offer high accuracy, their computational demands can be prohibitive. For this reason, we developed a software tool (written in C and Python) called 'REVOLT-U', which trades a small degree of accuracy for significant gains in simulation speed and resource demands. While more details can be found in [21–23], here we recall that, starting from the emissivity of the x-ray source, REVOLT-U calculates counts and energy spectra at each detector pixel, accounting for detector efficiency and x-ray attenuation. The source emissivity can be derived from independent simulations, experimental data, or computed directly by REVOLT-U using a simple Bremsstrahlung model [21, 24]. The code has been presented and validated in [21], using GEANT4 as a reference standard and MAST-U [25] experimental data from the MU-03 campaign [5].

In this work, REVOLT-U simulations were used extensively to adjust the design of the RFX-mod2 GEM

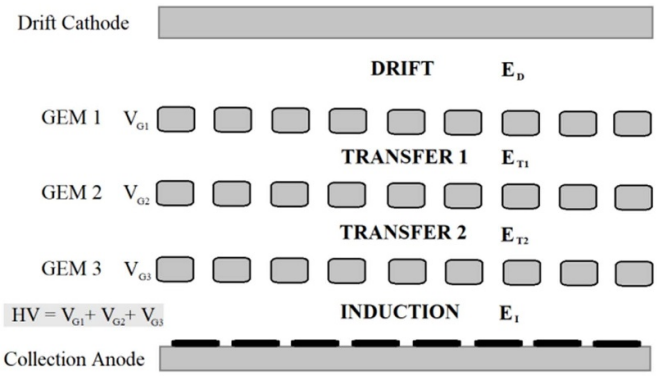

Figure 1. Diagram of a triple-GEM detector. HV is defined as the sum of the voltages applied to each GEM foil.

diagnostic and its line of sight, as well as to develop suitable algorithms for tomographic reconstruction of emissivity profiles. REVOLT-U additionally enables the integration of other Monte Carlo simulation tools, thereby enhancing the accuracy of detector response simulations. In this work, for example, Heed [26] was used to determine the number of primary electrons generated by simulated incident x-rays.

2. Diagnostic design: CAD model

RFX-mod2 has two available access ports for the allocation of the GEM diagnostic—an upper central port and an upper external port (located in the upper part of sector 12D of the vacuum vessel). Considering realistic constraints, the full diagnostic was designed on the basis of REVOLT-U simulation results (some of which are discussed in next sections of this paper).

The design features two GEM detectors housed within a single Faraday cage used to reduce electronic noise from electromagnetic interference.

At the detectors position, an intense stray magnetic field is expected, with a magnitude remaining below 200 mT at all times. Garfield++ [27] simulations were carried out to assess the effect of the magnetic field on the GEM physical detection mechanism. From a physical standpoint, simulations indicated that the presence of magnetic fields up to 200 mT do not impair the performance of GEM detectors, even when the magnetic field is assumed to be fully perpendicular to the velocity of electrons generating the signal. Consequently, it is expected that the detector electronics will be the limiting factor.

Thanks to the experience gained with a GEM detector installed at MAST-U [5], it was understood that the FPGA power supply system is the main source of problems, as it can shut down in the presence of strong magnetic field disturbances, resulting in the interruption of data acquisition.

A solution for the power supply system has been conceptualized, but will not be discussed here. A scientific article on the subject will follow this publication, illustrating the details of the Garfield++ simulations and the results of laboratory tests performed with a system that implements the conceptualized solution. This system will consist of placing the entire GEM detector (or just the GEM electronics) inside a large solenoid capable of reaching at least 500 mT. Rotating the GEM detector inside the solenoid will allow for the study of the effect of different magnetic field orientations.The diagnostic system is modeled in a full CAD representation obtained with CATIA [28]. The latter includes the RFX-mod2 assembly, flanges, gate valves, beryllium windows, and pinholes; constituting the detectors lines of sight. Helium buffers, the detectors with their electronics, and the Faraday cage are also included. More specifically, each detector line of sight features:

- An Helicoflex-CF63 adapter to allow compatibility with the helicoflex access ports of RFX-mod2.
- A CF63 gate valve with a CF63 flange on top to allow for intervention in case of vacuum leaks.
- Two CF16 outlets on each CF63 flange dedicated to a pressure sensor and a pumping system (for monitoring and evacuating the interspace between the gate valve and the CF63 flange).
- A 25 μm thick[7] beryllium x-ray exit window [29] (Be window) attached to an additional CF16 outlet in the CF63 flange.
- A motorized pinhole following the Be window.
- An helium buffer placed in the space between the Be window and the detector, joined with JACOB flanges on top and bottom.
- A rail-mounted cart for positioning the diagnostic box.
- The diagnostic box consisting of the Faraday cage housing the detectors and their electronics.

These components are indicated in figures 2 and 3, including the two GEM detectors, which will be referred to in the text as GEM 1 and GEM 2.

As shown in figure 3, each GEM detector has a rectangular shaped anode with dimensions 100 mm $\times$ 25 mm, divided into 64 $\times$ 2 channels.

The geometrical view cones of each detector are drawn in figure 4.

Each pinhole serves two primary functions: enhancing optical resolution by reducing image blurring and regulating the detector count rate. The helium buffer is needed to reduce x-ray attenuation. More details on the effect of the pinhole diameter and the helium percentage in the buffer are discussed in sections 3.2 and 3.3.

To allow full control on the pinhole diameter, a motorized pinhole consisting of two adjustable elliptical irises was

[7] The manufacturer [29] certifies that the selected beryllium windows maintain vacuum integrity up to a differential pressure of 2 atm (front pressure specification), with a maximum allowed leak rate of $<1 \times 10^{-10}$ mbar·l s^{-1}. Under RFX-mod2 operational conditions, the windows will experience a pressure difference of approximately 1 bar, with atmospheric pressure ($\approx$1 bar) on the external side and a pressure higher than 10^{-9} mbar (likely on the order of 10^{-8}–10^{-7} mbar) on the internal side. This operating condition is within the manufacturer's specifications. Furthermore, an identical beryllium window was successfully operated at the high voltage Padova test facility under comparable conditions ($P_{ext} \approx 1$ bar, $P_{int} \approx 10^{-7}$ mbar, $\Delta P \approx 1$ bar). On that occasion, x-ray measurements with a GEM detector were performed without faults or leaks [23].

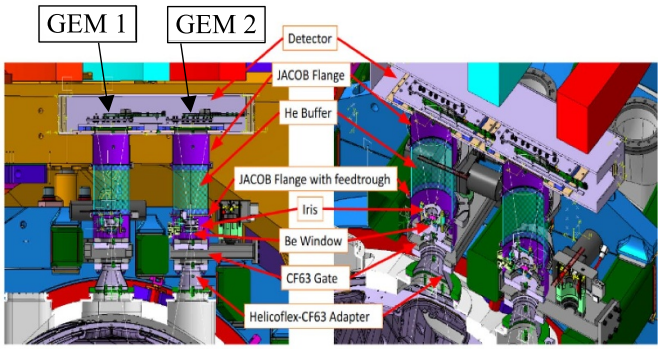

Figure 2. Full CAD drawing of the diagnostic line of sight. The main components of the line of sight are indicated with arrows. In the figure, 'detector' indicates the complete assembly comprising the Faraday cage, the GEM detectors and their electronics. With 'GEM 1', we refer to the detector positioned in correspondence to the central access port. With GEM 2, we refer to the detector positioned in correspondence to the external port.

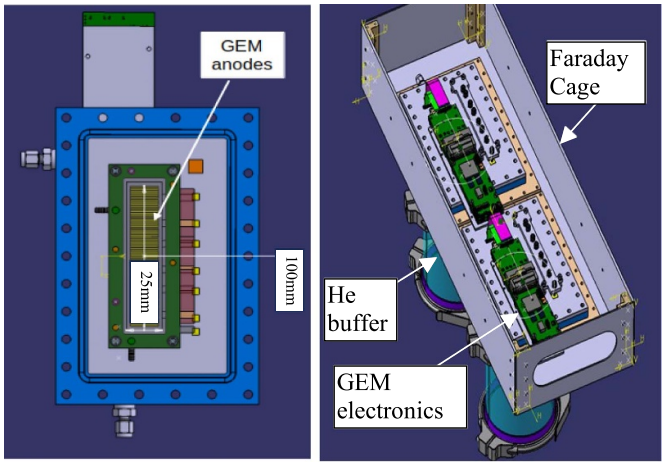

Figure 3. GEM detector design. On the left, the anodic pixels of a single GEM detector are shown. They are 64 × 2 anodic pixels, with a total width of 25 mm and a total height of 100 mm. On the right, the diagnostic assembly with the two detectors mounted inside the Faraday cage is shown.

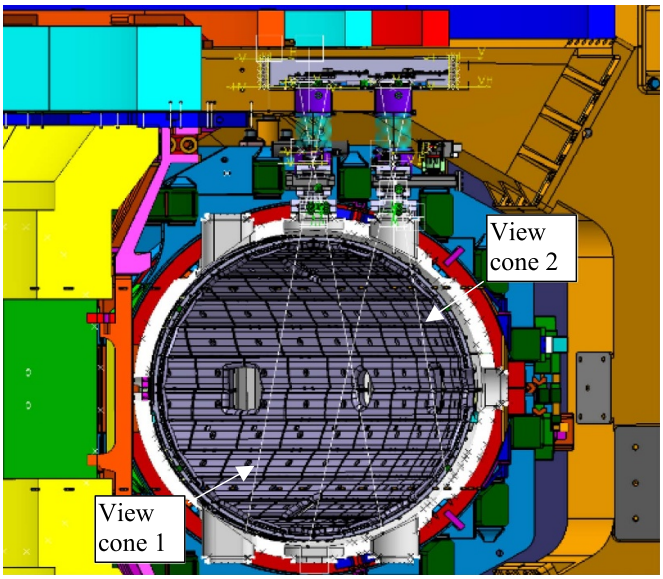

Figure 4. Poloidal section of RFX-mod2 CAD model. The GEM diagnostic view cones are represented in white. View cone 1 is the one associated to the GEM 1, view cone 2 is the one associated to the GEM 2.

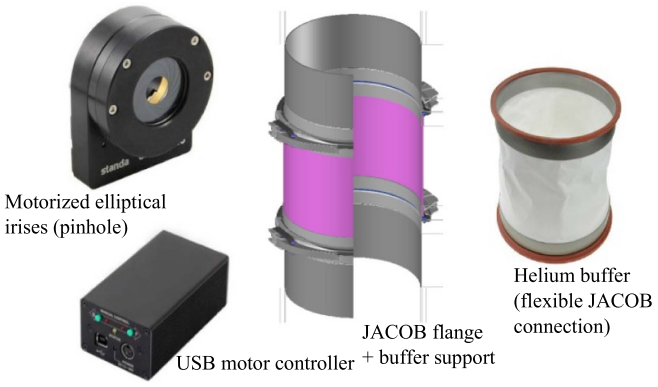

Figure 5. Pinhole and helium buffer components (discussed in the text).

chosen. The two irises forms an effective pinhole with an aperture resolution of 2.6 μm [30].

The foreseen helium buffers are flexible JACOB connections (FDM) [31] made of poly urethane with knitted polyester ply, having a low helium permeability. The helium buffer is housed in a tube serving as support structure, joined with JACOB flanges at the top and bottom. The bottom flange is modified to host the gas inlet pipe plus a USB feedthrough, while the top flange is modified to host the gas outlet pipe. The pinhole and helium buffer components are shown in figure 5.

The gas composition inside each helium buffer is not actively regulated via feedback control. However, the composition can be modified by adjusting the helium flow rate using a Bronkhorst flow meter [32] connected to a helium gas tank. The flow meter enables dynamic control of the gas flow rate. Therefore, the flow can be stopped and resumed as needed.

It has been proposed to install two ^{55}Fe laboratory sources, on the side of each pinhole. These sources would be used to monitor the gains of both detectors and the effective helium fraction within each helium buffer. To obtain a reference measurement, helium would be fluxed at a sufficiently high rate to reach a steady-state fraction that remains close to 100%. In this condition, the count rate at the full energy peak (∼6 keV for ^{55}Fe) would be measured. Any deviation from this reference value (after accounting for the source activity decay over time) would be indicative of a variation in the helium percentage. Indeed, the detection efficiency strongly depends on the gas composition in the buffer (see section 3.2).

The proposed method should allow for indirect yet effective monitoring of the helium percentage without requiring a

dedicated gas analyzer. If necessary, variations in the helium percentage can be compensated by adjusting the flow rate.

Another important aspect concerns the possible permeation of helium through the GEM detector window (12.7 μm thick aluminized Mylar). Since helium atoms can diffuse through the window material, a small fraction of helium may enter the detector volume, potentially altering the composition of the working gas and, consequently, the detector gain. To evaluate this effect, published data on helium permeation through aluminized Mylar [33] were used to estimate the steady-state helium fraction inside the detector. In this calculation, it was taken into account that the detector working gas is continuously flowed at a rate of 5 l h^{-1} (regulated by a Bronkhorst flow meter analogous to that planned for the helium buffers) [10]. The resulting steady-state helium fraction was found to be between 1 and 10 parts per million. A fraction of 10 parts per million was then used as input for Garfield++ [27] simulations. The latter showed no significant effect on the detector gain, as the gain difference was statistically consistent with zero (within one standard deviation). Despite this encouraging result, the ^{55}Fe sources would also be used to monitor the gain of each detector, aiming at long-term stability. Indeed, gain variations can arise not only from fluctuations in the gas composition, but also from fluctuations in the pressure, temperature and humidity of the working gas [34, 35]. The ^{55}Fe full-energy peak in the detectors' TOT spectra can be continuously monitored to identify any shifts indicative of gain variations. A feedback control system, similar to the one described in [36] is planned for implementation. This system should interpret peak shifts as gain variations and automatically adjust the detectors' high voltage to maintain the peak position (and therefore the detector gain) fixed within a predefined tolerance.

3. REVOLT-U simulations of RFX-mod2

3.1. Simulations description

To simulate SXR data on GEM detectors, the CAD model described above was used as reference for defining the geometry in REVOLT-U, following the procedure described in [21]. A schematic representation of the geometrical parameters used in the simulations is shown in figure 6.

In the actual system, each GEM detector will have an anode divided into 128 copper pads, each with an area of 1.56×12.5 mm^2, arranged in a matrix of 64×2 channels. However, during RFX-mod2 operations, the counts in the two *channels* along the short dimension will be added together, providing the equivalent of an effective 1D array detector of 64 *pixels*. This choice is made because it allows distributing the counts across two channels, thus reducing the probability of pileup [17].

In the REVOLT-U simulations presented in this work, each detector was represented as a 1D array of 64 pixels, each with dimensions 1.56 mm $\times$ 25 mm.

The x-ray source emissivity $\left(\frac{\mathrm{d}\tilde{N}}{\mathrm{d}E}\right)$ was modeled using the simple model built in REVOLT-U [21, 24], as described by equation (1):

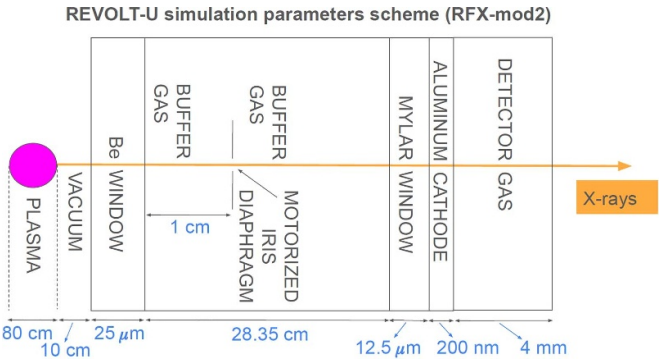

Figure 6. Schematic representation of the geometrical parameters used in the simulations presented throughout the main text. These parameters were derived from the CAD model presented in section 2.

$$\frac{\mathrm{d}\tilde{N}}{\mathrm{d}E}(E)\left[\frac{\#ph}{s\,m^3\,eV}\right] = \varsigma\left[\frac{\#ph\,eV^{1/2}\,m^3}{s}\right] \times \frac{Z_{\mathrm{eff}}\,{n_e}^2\left[\mathrm{m}^{-6}\right]}{T_e^{1/2}\left[eV^{1/2}\right]}\,\frac{e^{-\frac{E[eV]}{T_e[eV]}}}{E[eV]}, \tag{1}$$

where:

- $\frac{\mathrm{d}\tilde{N}}{\mathrm{d}E} = \frac{\mathrm{d}N}{\mathrm{d}t\,\mathrm{d}V\,\mathrm{d}E}$ is the number of photons emitted by the plasma source per unit time, volume and photon energy.
- n_e is the electron density.
- T_e is the electron temperature.
- is an effective atomic number that represents the average ion charge state: $Z_{\mathrm{eff}} = \frac{\sum_i n_i Z_i^2}{\sum_i n_i Z_i} = \frac{\sum_i n_i Z_i^2}{n_e}$, where i indicates the ionic species and n_i and Z_i their densities and atomic numbers. For the second equality, quasi-neutrality is assumed.
- ς is a global multiplying parameter obtained by fitting REVOLT-U synthetic data to experimental data.
- The measurement units are displayed inside squared brackets for each term of the equation. '#ph' reads 'number of photons'.

In [21], a fit parameter was determined through the comparison of REVOLT-U synthetic data with experimental measurements from a specific MAST-U session. In that work, the fit results were reported in terms of a parameter (indicated with 'α') that was multiplied to the synthetic counts of each detector pixel (with α maintained constant across all pixels). However, since REVOLT-U calculates detector counts through linear operations starting from the emissivity spectrum, the fit parameter can be brought inside summation and integral signs and be multiplied directly to the emissivity spectrum used initially to obtain the synthetic data. The result of the multiplication is the global multiplying parameter ς shown in equation (1).

Here, we present the same fit results from [21], but expressed in terms of ς:

$$\varsigma = (2 \pm 1) \times 10^{-20}.$$

In [21], it was shown that maintaining the value of α (which corresponds to the value of ς displayed above) constant, resulted in consistent agreement between experimental

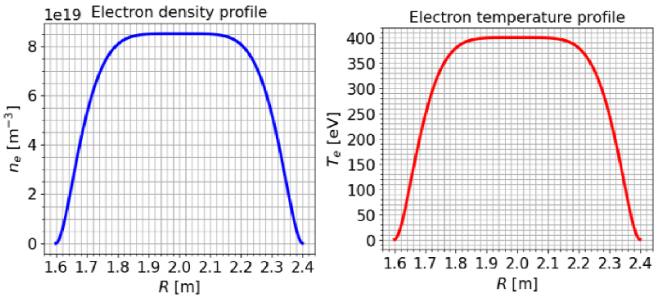

Figure 7. Radial profiles of electron density and temperature used for the thermal component of the simulated SXRs.

and simulated data across multiple experimental sessions of MAST-U. At the time of the present work, RFX-mod2 data are not yet available since device operations are not yet started. Therefore, the value of ς was assumed to be equal to 2×10^{-20}, as this represents the only available result from a SXR GEM detector developed by our team and installed in a fusion device. However, once the RFX-mod2 experimental campaign begins, the value of ς should be recalculated through a fitting procedure similar to that described in [21], and the simulations should be updated accordingly.

The primary objective of this paper is to present the capabilities of the software and data analysis framework we have developed by showing how they have been used to design the SXR GEM diagnostic tailored for RFX-mod2, rather than to present definitive and reliable absolute detector count predictions. This limitation has been acknowledged and was a principal motivation for developing a flexible diagnostic design incorporating motorized pinholes and helium buffers (see section 2), which enable broad-range adjustments to accommodate possible discrepancies (even substantial ones) between simulated and experimental photon fluxes incident on the detectors.

The radial T_e and n_e profiles used for the simulations of this paper are reported in figure 7. As done in [21], Z_{eff} was assumed to have a constant profile along the radial coordinate ($Z_{eff} = 1.5$ for all values of R). Throughout the text, this configuration will be referred to as '400 eV configuration'.

Starting from the x-ray source emissivity, REVOLT-U calculates counts and energy spectra at the pixels of each GEM detector described in section 2.

The procedure to obtain these synthetic data is described in detail in section 2 of [21]. It accounts for the detector efficiency, the shadowing effect from experimental components, and the x-ray attenuation through the beryllium window and the gas mixture inside the helium buffer. It assumes that each detector event [17] results in a count, ignoring detector dead time and pileup events.

3.2. Effect of the helium purity in the buffer on energy spectra and count rates

Each helium buffer foreseen for RFX-mod2 allow to reduce x-ray attenuation through air, providing two main advantages:

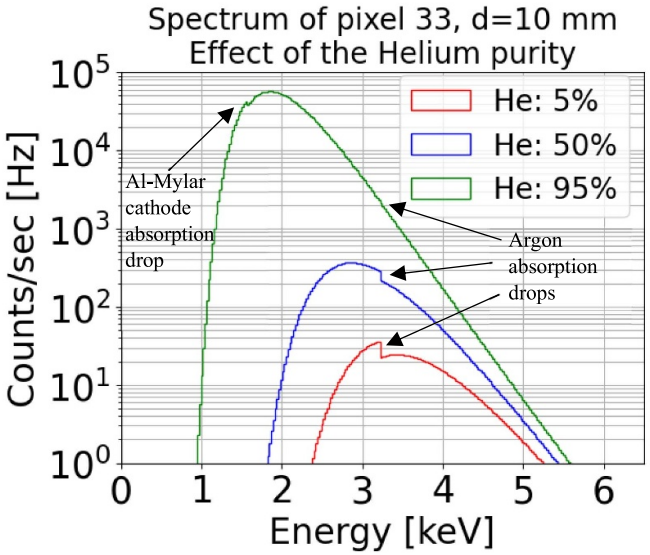

Figure 8. Effect of the helium purity on the energy spectrum at the detector. The starting point of the energy spectrum shifts to the left as low energy photons are able to pass through helium without being absorbed. The count rate increases by orders of magnitude with the helium purity. This figure was obtained considering a simulation of GEM 1, with Ne/CO_2–70/30% gas mixture, pinhole diameter d = 10 mm, and the 400 eV plasma configuration. Absorption drops are discussed in the text.

1) It shifts the energy spectrum starting point (at the detector) towards lower energy values, thus broadening the energy range to possibly perform a fit for the estimation of the electronic temperature [5] from the energy spectrum.
2) It increases the photon flux reaching the detectors, thereby reducing measurement errors thanks to enhanced count statistics.

Both features can be seen from the energy spectra of figure 8, which shows synthetic spectra obtained with REVOLT-U in a central pixel of GEM 1. The detector gas mixture was Ne/CO_2–70/30%, the pinhole diameter was set to 10 mm, while the helium percentage in the buffer was varied. In RFX-mod2 experiments, the helium percentage will be adjusted using the flow meter described in section 2. Looking at figure 8, the drop at 3.2 keV is due to the Argon absorption peak (due to the presence of Argon in air). Therefore, it decreases if the air percentage in the buffer decreases. One could think that this is another advantage of increasing the helium fraction in the buffer, however, these simulations do not consider the detector resolution and the statistical errors. They only consider the theoretical detector efficiency (as described in section 4 of [21]). Therefore, in practice, finite detector resolution and statistical count fluctuations would likely blur or erase this feature in experimental data, even though no helium buffer is present. The drop at 1.5 keV, visible only for the spectrum with the higher helium purity, is due to the absorption of SXR by the GEM cathode (made of aluminized Mylar). However, REVOLT-U does not simulate fluorescence x-rays, which could play a role in modifying that

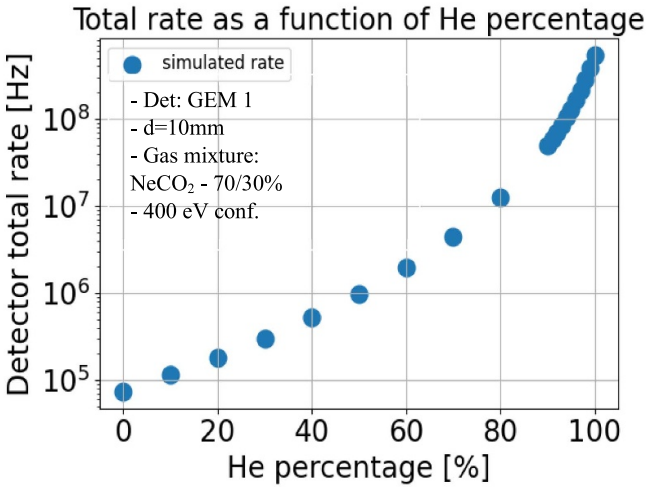

Figure 9. Total detector count rate (sum of rates from every pixel, integrated over all photon energies) as a function of the helium percentage. The count rate increases by 4 orders of magnitude in passing from 0% to 100% helium purity in the helium buffer. This figure was obtained considering a simulation of GEM, with Ne/CO_2–70/30% gas mixture, pinhole diameter d = 10 mm, and the 400 eV plasma configuration.

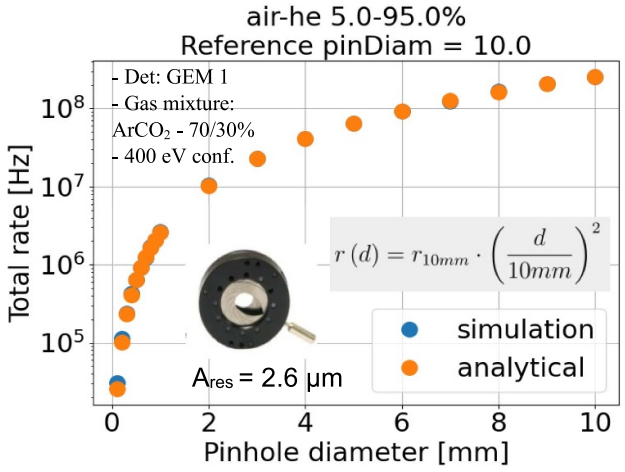

Figure 10. Detector count rate (sum of rates from every pixel, integrated over all photon energies) as a function of the pinhole diameter d. The count rate increases by 4 orders of magnitude in passing from d = 0.1 mm to d = 10 mm. The figure also shows the analytical formula used to calculate the rate as a function of the pinhole diameter, a picture of the pinhole that is foreseen for installation and its aperture resolution A_{res}. r and r_{10mm} represent the rate obtained with pinhole diameter d and 10 mm, respectively. This figure was obtained considering a simulation of GEM 1, with Ar/CO_2–70/30% gas mixture and an helium percentage in the buffer equal to 95%.

structure. In addition, the energy resolution and count statistics would smooth out this structure as well.

As previously mentioned, the number of photons reaching the detectors increases with the helium purity. In fact, they can increase so much that a pinhole becomes necessary to reduce the detector count rate to acceptable values in terms of GEM rate capability (≈1 MHz/pixel) and detector current limit (≈20 μA). The effect of the helium purity on the total detector count rate is shown in figure 9. The total rate is defined as the sum of rates in all detector pixels and considering all incident photon energies. The rate increases by 4 orders of magnitude for helium percentage going from 0% to 100%.

3.3. Effect of the pinhole diameter on the count rate at the detector

During experiments, obtaining 100% helium purity could be challenging. Therefore, for simulations, we select a more realistic helium percentage of about 95%. Figure 8 shows that this value is sufficient to achieve an energy spectrum starting point at about 1 keV. Lowering the starting point would be unnecessary due to the GEM electronics threshold that allows for noise pulses rejection: pulses with energy below ≈1 keV are identified as noise and discarded. The detector count rate at 95% helium purity is higher than the detector rate capability. Therefore, a pinhole is necessary to reduce the count rate. The pinhole foreseen for installation at RFX-mod2 has a diameter that can be varied during experiments thanks to the use of a motorized mechanism. The pinhole (figure 10) consists of two elliptical irises which closes in combination to create an effective aperture of given dimension. In this way, it can reach an aperture resolution of 2.6 μm [30]. The effect of the pinhole diameter on the detector counts is purely geometrical and it is due to the reduction of effective x-ray acceptance area in the line of sight. Figure 10 confirms this by showing that the simulated rates closely match those derived analytically using equation (2):

$$r(d) = r_{10\text{mm}} \cdot \left(\frac{d}{10\text{mm}}\right)^2 \tag{2}$$

where $r(d)$ and $r_{10\text{mm}}$ represent the rate obtained with pinhole diameter d and 10 mm, respectively.

A small discrepancy is seen only for pinhole diameters smaller than 0.3 mm due to REVOLT-U voxel dimensions becoming comparable with the pinhole diameter. The problem was mitigated by simulating REVOLT-U plasma with more (thus smaller) voxels. This, however, requires a higher computational demand. Figure 10 uses an $ArCO_2$ gas mixture; however, since the pinhole's effect is purely geometrical, equation (2) and the associated considerations remain valid for detectors using Ne/CO_2 as well.

During RFX-mod2 experiments, the He percentage will likely remain fixed at the higher achievable value, while the pinhole diameter will be adjusted for different plasma pulses depending on their target scenario, e.g. tokamak configuration, multiple helicity (MH), quasi single helicity (QSH), the presence of the diagnostic neutral beam and/or strong magnetic reconnection events. Reducing the pinhole diameter also minimizes image blur, thereby enhancing the optical resolution of the detector. This advantage supports using maximum helium purity in the buffer, as it allows for further diameter reduction without compromising x-ray transmission.

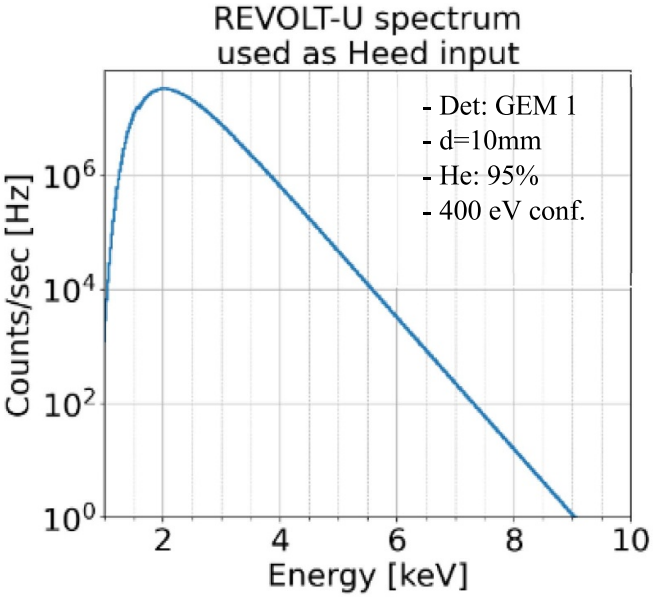

Figure 11. Example of input spectrum to Heed's function for current calculation. It represents the energy spectrum of photons immediately after the aluminized-Mylar cathode of GEM 1.

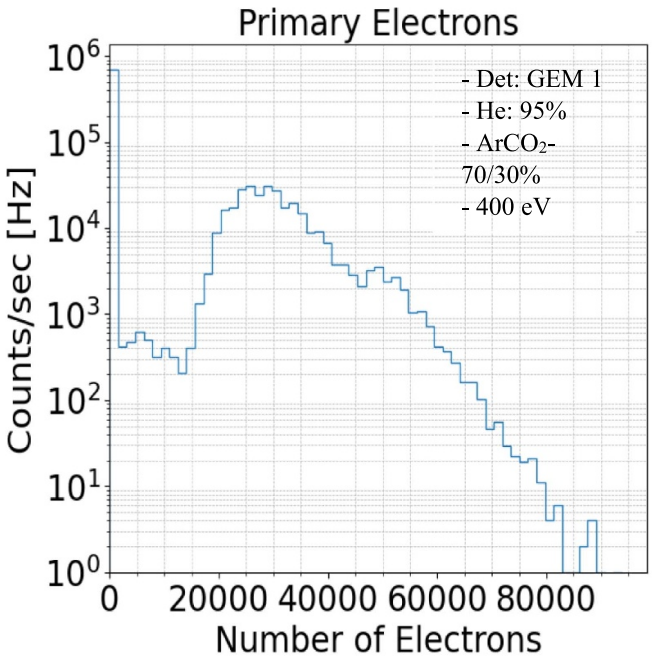

Figure 12. Example of spectrum of primary electrons calculated with Heed, using the spectrum of figure 11 as input.

4. Detector current as a function of experimental knobs

Excessive count rates not only exceed the rate capability of the GEM detector, but can also induce excessive currents that can compromise its integrity. On the other hand, a low count rate results in large statistical errors and lost of important information. Therefore, during experiments, the goal is to maximize the count rate while remaining below the limits imposed by the detector rate capability and the maximum allowable detector current. To achieve this, it becomes useful to estimate the current in the detector as a function of 'experimental knobs', namely the pinhole diameter and the cumulative high voltage applied to the GEM foils (indicated as *HV* in figure 1). While the count rate can be directly obtained from REVOLT-U simulations and compared with the rate capability limit of ≈1 MHz/pixel, calculating the detector current requires a different approach:

The energy spectrum (counts/second) of photons immediately after the Aluminized-Mylar cathode is simulated with REVOLT-U. An example is shown in figure 11.

- This spectrum is used as input to a program that uses Heed [26] to calculate the resulting number of primary electrons per second ($r_{\mathrm{p}}^{\mathrm{tot}}$). In particular, for each energy bin of the spectrum, the drift of $H(E)$ photons having an energy randomly extracted from $U\left[E-\frac{\Delta E}{2}, E+\frac{\Delta E}{2}\right]$ is simulated. $H(E)$ is the height of a bin of the input spectrum with central energy E and width ΔE.

  Each photon, indexed by i, generates a discrete number of primary electrons (N_{p}^{i}) in the simulation. Figure 12 shows an example of the resulting primary electron spectrum. The total rate of primary electrons produced by all photons is therefore given by:

$$r_{\mathrm{p}}^{\mathrm{tot}} = \sum_{i=1}^{N_{\mathrm{ph}}} N_{\mathrm{p}}^{i}$$

where N_{ph} is the number of photons that were simulated. The total rate of primary electrons $r_{\mathrm{p}}^{\mathrm{tot}}$ is used to calculate the total detector current I_{tot} through equation (3):

$$I_{\mathrm{tot}} = r_{\mathrm{p}}^{\mathrm{tot}} \cdot G \cdot e \tag{3}$$

where $e = 1.602 \times 10^{-19}\mathrm{C}$ is the elementary charge in Coulomb and G is the effective gain of the detector, i.e. the ratio between the detected charge and the primary ionization charge [9]. G is an exponential function of HV and is determined experimentally. The measured values of $G(HV)$ for a GEM detector using an Ar/CO_2–70/30% gas mixture were published in [37] and are shown in figure 13, along with an exponential fit (equation (4)).

$$G = a \cdot e^{b \cdot HV} \tag{4}$$

where a and b are the fit parameters. These are only reference measurements, used here to illustrate the calculation procedure that will be used for RFX-mod2. However, during the detector characterization and calibration phase, measurements of G as a function of HV for Ar/CO_2–70/30% and Ne/CO_2–70/30% gas mixtures will be performed directly by us.

Since the rate as a function of the pinhole diameter (d) is known (equation (2) and $G(HV)$ is known (equation (4)), the last ingredient that we need to express the detector current in terms of HV and d is the formula that relates the input rate to the detector current. To obtain the latter, the input spectrum

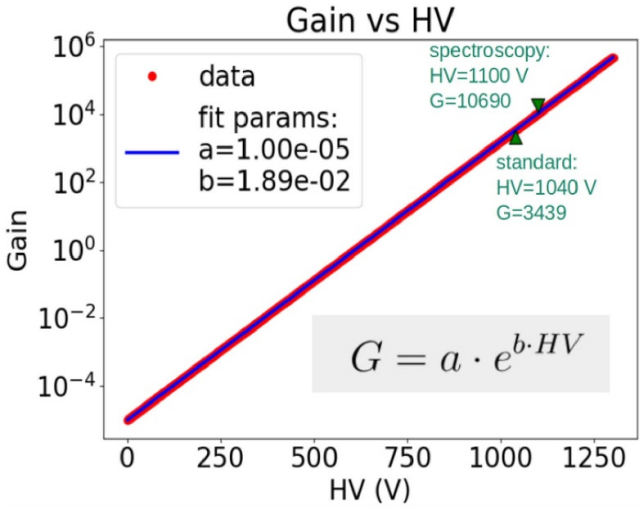

Figure 13. Gas effective gain G as a function of HV for the Ar/CO_2–70/30% gas mixture.

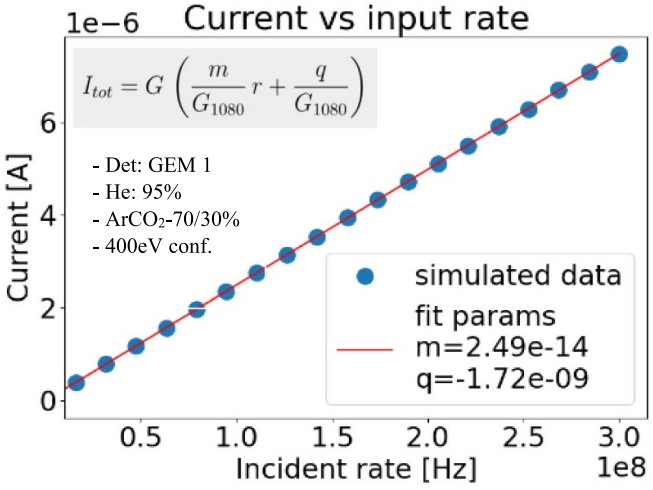

Figure 14. Detector current as a function of the total incident rate (calculated as the integral of the input spectrum). The way the different rates are obtained is discussed in the text.

of figure 11 is multiplied by different scaling constants to achieve different values of total incident rate. Then, each resulting spectrum is given as input to the Heed function to obtain the corresponding detector current. This procedure is equivalent to run several simulations with different pinhole diameters, but allow for a reduction in computational time and resource consumption. Figure 14 shows the resulting current I_{tot} as a function of the input rate r. A linear fit with unknown parameters m and q is superimposed to simulated data:

$$I_{tot} = m \cdot r + q \tag{5}$$

The fit parameters were calculated for a specific value of effective gain ($G_{1080} = 7325$) and $HV = 1080$. However, since equation (3) tells us that I_{tot} is proportional to G (under the assumption of working at the calibration curve plateau), to generalize the fit results for different values of G is sufficient to use equation (6):

$$I_{tot} = G\left(\frac{m}{G_{1080}} \cdot r + \frac{q}{G_{1080}}\right) \tag{6}$$

which is the one shown in figure 14.

Putting together all these ingredients, the overall equation describing the current as a function of experimental knobs is:

$$I_{tot}(d, HV) = a \cdot e^{b \cdot HV} \cdot \left(\frac{m}{G_{1080}} \cdot r_{10mm} \cdot \left(\frac{d}{10mm}\right)^2 + \frac{q}{G_{1080}}\right) \tag{7}$$

where is the gain for Ar/CO_2 at $HV = 1080$. Having this formula should allow the selection of values of d and HV close to the optimal ones, reducing the number of trial-and-error adjustments during plasma operations. For the first RFX-mod2 plasma discharges, a cautious approach will be adopted, starting from low values of HV and d, in order to assess the discrepancy between the model predictions and the measured detector currents before relying on it.

Lastly, it is important to highlight that the shape of the input spectrum is fixed in this calculation and is determined by the simulated source emissivity ('400 eV configuration' in this case). Choosing a different detector gas mixture, different access ports (i.e. GEM 1 and GEM 2), different Plasma configurations, or different helium percentages in the buffer, results in different numerical values for the fit parameters of equation (7). However, its functional form remains the same. Simulations must be run multiple times to determine the fit parameters and, therefore, the current laws for all possible configurations of interest. In the specific configuration discussed here as example, the estimated detector current for a pinhole diameter $d = 10$ mm and $HV = 1080$ V was $I_{tot} = 10.62$ μA, while the detector rate overcomes the limit of 1 MHz/pixel. Therefore, the detector rate capability is the limiting factor in this particular case. On the other hand, in a plasma scenario with 1 keV electron temperature or in case of high energy electron population leading to high energy tails in the SXR spectrum, the detector current increases. This occurs because higher-energy photons produce more primary electrons per interaction. Therefore, in those cases, the current can become the limiting factor rather than the detector rate capability.

5. Emissivity profile reconstruction resolved in energy

5.1. Emissivity profile reconstruction algorithm

A tomographic reconstruction algorithm was developed to perform tomographic reconstructions of plasma SXR emissivities. The algorithm is based on the Tikhonov procedure to solve ill-posed problems and has been developed following our previous work on experiments at the high voltage Padova test facility [23].

Initially, the algorithm was designed to perform reconstructions of full two-dimensional (2D) emissivities representing poloidal sections of the plasma. However, since only two vertical access ports are available at RFX-mod2, full 2D

reconstructions becomes unfeasible with that algorithm (it would require at least two detectors placed at about 90° relative angle). Nevertheless, it was found that the same procedure works very well for determining *profile reconstructions* of plasma emissivity, provided that the 2D reconstruction is integrated along the vertical dimension.

Even though 2D reconstruction are not currently feasible with this diagnostic configuration, emissivity profile reconstructions with GEMs would likely remain a valuable information for RFX-mod2 experiments, especially considering that they will also offer photon energy discrimination. Indeed, it is worth noting that another SXR diagnostic, based on photodiodes and tailored for 2D tomographic reconstruction, will be installed at RFX-mod2. This diagnostic will feature 58 lines of sight located in different poloidal portholes at the same toroidal section and it has already demonstrated its performance in RFX-mod past experiments [2, 7]. However, its main limitation is that it does not offer energy-resolved measurements. Therefore, in this context, the GEM diagnostic should serve as a complementary tool to the photodiode tomographic system, offering energy-resolved measurements of emissivity profiles with ≈1 cm spatial resolution.

The procedure to obtain emissivity profile reconstructions with the GEM diagnostic is briefly summarized in the following section. Calling ϵ_{2D} the 2D emissivity in a plasma poloidal section, the Tikhonov method [38] consists in searching the value of ϵ_{2D} that minimizes the following cost function:

$$\text{cost}\left(\epsilon_{2D}\right) = \left|\mathbf{L}\cdot\epsilon_{2D} - S\right|^2 + \lambda\left|\mathbf{C}\cdot\epsilon_{2D}\right|^2 \tag{8}$$

where $\mathbf{L}$ is the matrix that project the emissivity of each voxel to counts in each detector pixel. $\mathbf{L}$ is calculated using the REVOLT-U $\mathbf{SF_{3D}}$ tensor (see [21]). S is the array whose entries represent the counts in each detector pixel (wether experimental or synthetic), λ is the regularization parameter, and $\mathbf{C}$ is the constraint matrix, i.e. the matrix representing the application of constraints to ensure problem-specific properties. In this case, $\mathbf{C}$ represents the application of the Laplace operator (which ensures that the solution maintains a certain level of smoothness) with von Neumann boundary conditions [38–40]. ϵ_{2D} is a function of R and Z. The latter represent the radial and vertical locations of the REVOLT-U voxels.

ϵ_{2D} was found to not match well the true plasma emissivity (i.e. the input source used to generate synthetic data). However, integrating it along the Z axis leads to emissivity profiles $\epsilon_{1D}\left(R\right)$ that match well with those calculated from the true emissivity. The integration that leads from the 2D emissivity to the radial profile is reported in equation (9):

$$\epsilon_{1D}\left(R\right) = \int_{Z_{min}}^{Z_{max}} \epsilon_{2D}\left(R,Z\right)\,\mathrm{d}Z \tag{9}$$

where Z_{min}, Z_{max} represents the plasma boundary along the vertical coordinate (approximately 0.4 m and −0.4 m, respectively, for RFX-mod2).

An example of emissivity profile reconstruction starting from a complex shape emissivity of past RFX-mod data is discussed in section 5.2.

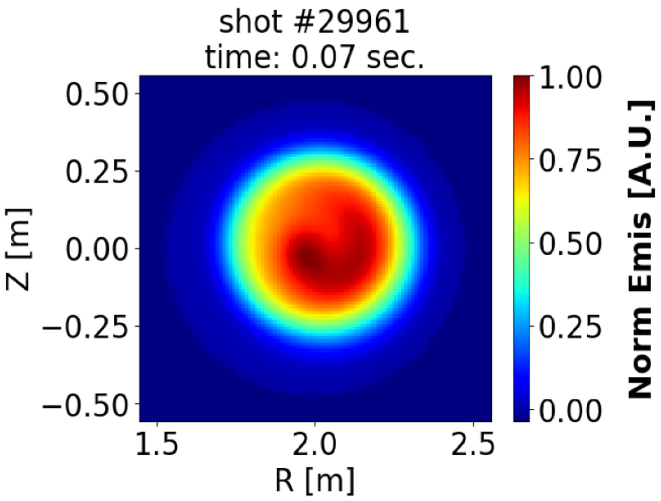

Figure 15. Normalized emissivity of RFX-mod shot #29961, at time = 70 ms, reconstructed with the SXR tomographic diagnostic based on photodiodes.

Since GEM detectors allow measurements resolved in energy, the variable S of equation (8) is actually a function of the photon energy E. The plasma emissivity is a function of energy as well. This can be understood by looking at equation (1), even though, in actual plasmas, the dependence of the emissivity on energy can be more complex.

By integrating GEM counts over narrow energy intervals and performing multiple minimizations of equation (8), it is possible to reconstruct emissivity profiles in a given energy range of interest. Section 5.3 discusses this procedure and provides an illustrative example.

5.2. Example reconstruction of past RFX-mod data

In past RFX-mod experiments, several measurements have been performed with the SXR tomographic diagnostic based on photodiodes. During MH states of RFX-mod, it was observed that the core of the plasma was stochastic due to the simultaneous presence of several instabilities. In this state, SXR emissivity reconstructions had a typical bell-shaped form. On the other hand, when the plasma reached QSH states, clear $m = 1$ structures were present in the brightness profiles, resulting in more complex shapes from the point of view of tomographic reconstruction [41]. We tested our emissivity profile reconstruction algorithm with several phantom emissivities created with REVOLT-U. At this stage, most of them were bell-shaped or simpler (e.g. emission form only a single voxel, all voxels emitting an emissivity equal to 1, etc). Then, for the last test phase, we used RFX-mod emissivities from past tomographic reconstructions. We used both data related to MH and QSH states. This section illustrates an example test using QSH data with complex shape. The purpose is to assess the algorithm's performance under challenging conditions, thereby providing insight into its robustness for difficult reconstruction tasks. The RFX-mod shot considered is the #29961, at time = 70 ms, and is shown in figure 15.

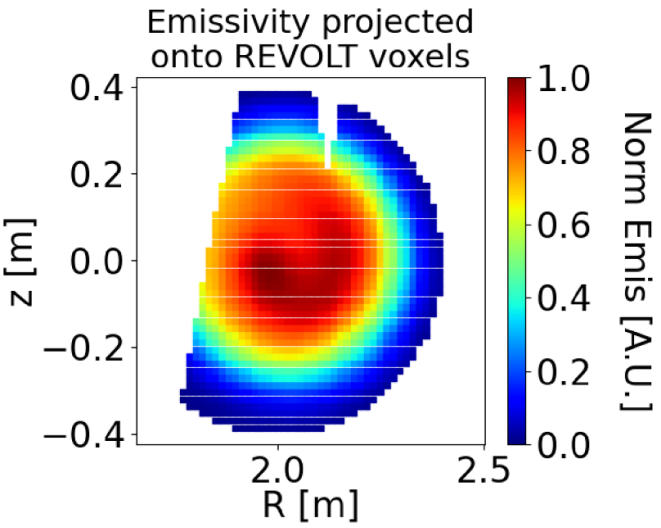

Figure 16. Past RFX-mod emissivity (figure 15) projected onto REVOLT-U voxels to create synthetic data. The emissivity boundaries are determined by the view cones of GEM 1 and GEM 2.

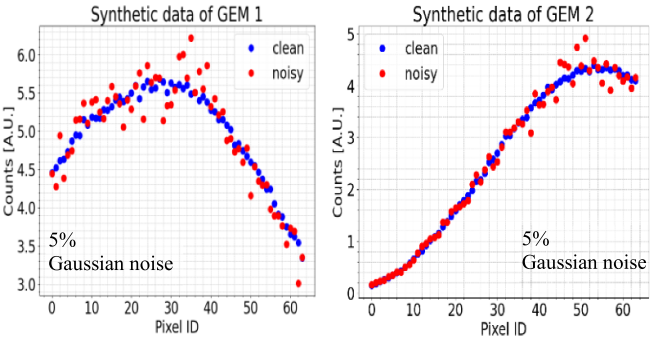

Figure 17. Clean and noisy synthetic data of GEM 1 and GEM 2, calculated with REVOLT-U using the source emissivity shown in figure 16. The way noise was calculated is described in the text.

To create the source emissivity for synthetic GEM detectors data, the emissivity of figure 15 was projected onto REVOLT-U voxels. The result is shown in figure 16.

The REVOLT-U voxels were initially defined as 50 along R and 50 along Z. Then, the program removed those that do not contribute to detector counts. Therefore, the emissivity boundaries in figure 16 were determined by the lines of sight of GEM 1 and GEM 2. REVOLT-U was used to calculate the counts at GEM 1 and GEM 2 starting from the emissivity of figure 16. The synthetic counts are shown in figure 17, both with and without synthetic noise. The latter was obtained by substituting the detector counts in each pixel i (indicated as S_i) with a random value extracted from a Gaussian distribution centered at S_i, and with the standard deviation defined by equation (10):

$$\sigma = \beta \cdot S_i \tag{10}$$

In this example, $\beta = 5\%$. This is indicated as '5% Gaussian noise' in figure 17.

Having called S the array containing all synthetic detector counts *with noise*, the cost function of equation (8) was

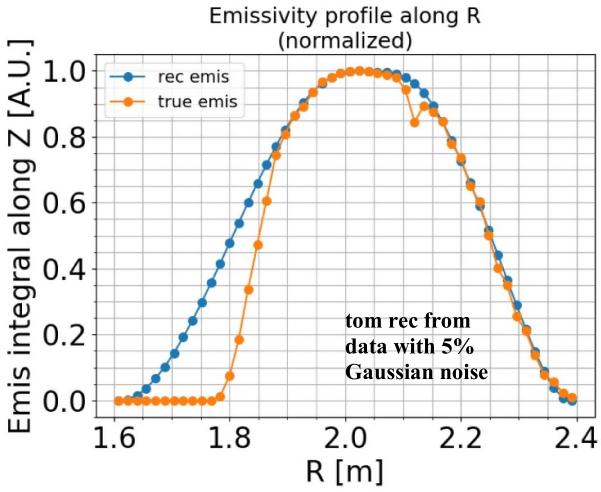

Figure 18. Reconstructed and true emissivity profiles of RFX-mod shot #29961, time = 70 ms. The reconstruction was performed considering data with 5% Gaussian noise (figure 17). The discrepancy at $R < 1.9$ m and $R \in [2.1, 2.15]$ m is due to the limited view cones of GEM 1 and GEM 2.

minimized to find ϵ_{2D}. The latter was used in equation (9) to obtain the reconstructed emissivity profile ϵ_{1D}^{rec}. ϵ_{1D}^{rec} is visually compared with the true emissivity profile (ϵ_{1D}^{true}) in figure 18.

Since REVOLT-U voxels were 50 along R (extending from 1.6 m to 2.4 m) and 50 along Z (extending from -0.4 m to 0.4 m), the reconstruction had a spatial resolution of 1.6 cm in this case. In principle, the latter can be improved by increasing the number of voxels in REVOLT-U. However, having fixed the number of detector pixels and its active area, the actual information content of the measurements is limited. Therefore, while a small increase can be beneficial, defining too many voxels (relative to the number of detector pixels) can lead to a computationally expensive problem with limited practical advantage in terms of spatial resolution.

A quantitative comparison of ϵ_{1D}^{rec} with ϵ_{1D}^{true} is shown in figure 19, where residuals are plotted against the radial coordinate. The residuals are defined by equation (11), and allow to assess the reconstruction accuracy,

$$\mathrm{res}\,(R) = 100 \cdot \left|\epsilon_{1D}^{rec}(R) - \epsilon_{1D}^{true}(R)\right| \tag{11}$$

The discrepancy between the reconstructed and the true emissivity profile is maximum at $R < 1.9$ m and $R \in [2.1, 2.15]$ m due to the true emissivity boundaries created by the limited view cones of the GEM detectors (see figure 16). Thanks to the regularization imposed on the solution by the reconstruction algorithm, the reconstructed emissivity profile is probably closer to the real one (figure 15) with respect to ϵ_{1D}^{true}, since the latter features a sudden decay due to the view cones limits. Nevertheless, to ensure reliability in experiments, reconstructions can be discarded at radial positions where the view cones do not fully cover the poloidal section (i.e. $R < 1.9$ m and $R \in [2.1, 2.15]$ m in this case).

Excluding these regions, the discrepancy between ϵ_{1D}^{true} and ϵ_{1D}^{rec} remains $\leqslant 4\%$ for all other radial positions, demonstrating

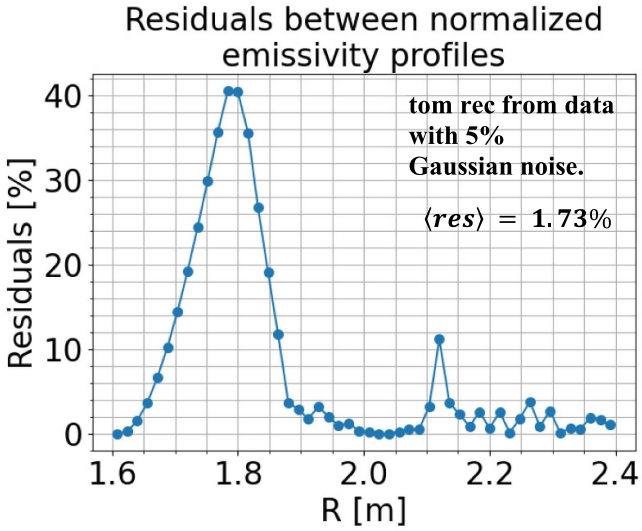

Figure 19. Residuals between the reconstructed emissivity and the true emissivity (both shown in figure 18). Average residuals (equation (12)) are also displayed.

the high accuracy of the reconstruction algorithm. To quantitatively evaluate the reconstruction with a single numerical value, we used the average residual as a figure of merit:

$$\langle \mathrm{res} \rangle = \frac{1}{N} \sum_{i=1}^{N} \mathrm{res}\left(R_i^{1.9}\right) \tag{12}$$

where $R_i^{1.9}$ are the radial positions corresponding only to $R > 1.9$ m, and N is their number. The result is displayed in figure 19.

At this point it is important to note that, even though the emissivity shape of figure 16 is complex, its emissivity profile (figure 18) is bell-shaped and therefore easier to reconstruct by an algorithm that imposes smoothness on the solution. Therefore, to test the algorithm even further, the emissivity of each voxel was elevated to the power of $\gamma = 10$, resulting in an enhancement of the image contrast. In other words, this procedure allowed to enhance the relative difference between more and less emissive voxels, with the result of producing a more complex radial profile. The result is shown in figure 20.

Elevating the voxel emissivity to maintains the emissivity unchanged. Therefore, to allow distinction of the two phantom emissivities throughout the rest of the text, we will indicate the emissivity of figure 15 as the one with $\gamma = 1$.

The source emissivity of figure 20 was used in REVOLT-U to generate synthetic detector data. Once again, 5% Gaussian noise was added before performing the reconstruction. Noisy and clean data are shown in figure 21.

Calling S the array containing all synthetic detector counts *with noise*, the cost function of equation (8) was minimized to find ϵ_{2D}. The latter was used in equation (9) to obtain the reconstructed emissivity profile (ϵ_{1D}^{rec}). ϵ_{1D}^{rec} is visually compared with the true emissivity profile (ϵ_{1D}^{true}) in figure 22.

A quantitative comparison is done in figure 23, where residuals are plotted against the radial coordinate.

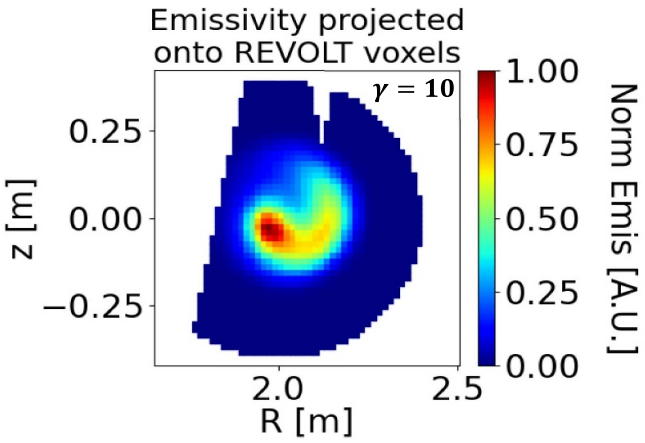

Figure 20. Emissivity of figure 16 enhanced by $\gamma = 10$. The emissivity boundaries are determined by the view cones of GEM 1 and GEM 2.

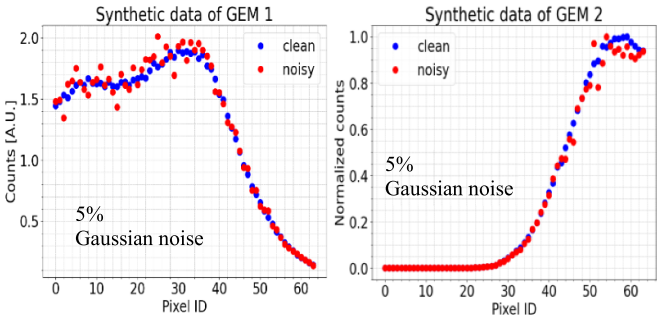

Figure 21. Clean and noisy synthetic data of GEM 1 and GEM 2, calculated with REVOLT-U using the source emissivity shown in figure 20. The way noise was calculated is described in the text.

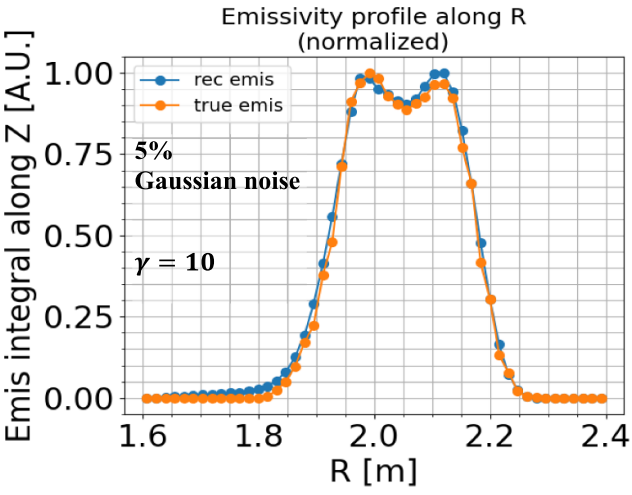

Figure 22. Reconstructed and true emissivity profiles of RFX-mod shot #29961, time = 70 ms, enhanced by $\gamma = 10$. The reconstruction was performed considering data with 5% Gaussian noise (figure 21).

In this case, several fluctuations on residuals are present due to the increased complexity in the emissivity profile shape. Nevertheless, the residuals remain below 8% for all radial

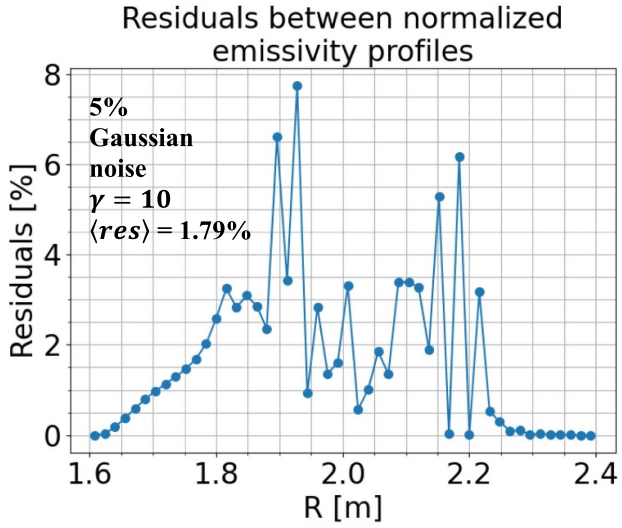

Figure 23. Residuals between the reconstructed emissivity and the true emissivity (both shown in figure 22). Average residuals (equation (12)) are also displayed.

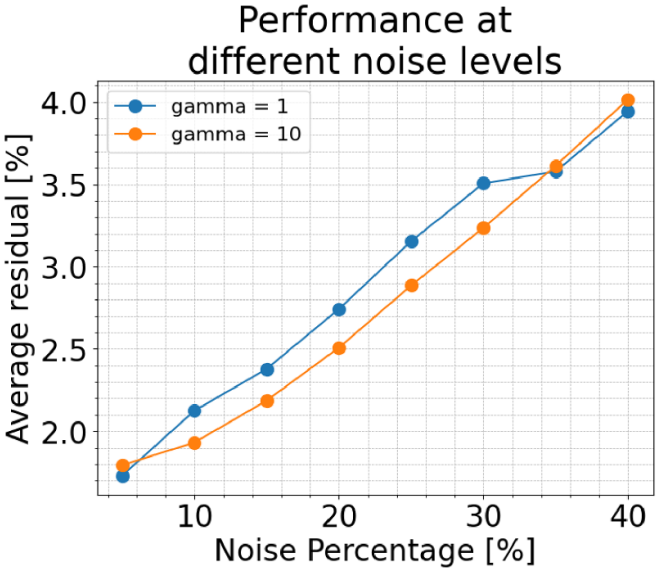

Figure 24. Average residual (equation (12)) against the noise level (i.e. β of equation (10)), for both the $\gamma = 1$ and cases.

positions, indicating good accuracy also in this case. The average residual is equal to 1.79%, compared to 1.73% of reconstruction in the $\gamma = 1$ case, providing additional evidence in favor of the previous statement.

In this case, discrepancies at $R < 1.9$ m and $R \in [2.1, 2.15]$ m are less critical than in the $\gamma = 1$ case. This is because the emissivity of external voxels is negligible compared to the emissivity of internal ones, effectively localizing the emissive region in a portion entirely seen by the GEM detectors. This can be seen by looking at figure 20. Nevertheless, the average residuals were still calculated considering only values of $R < 1.9$ m to allow for a comparison between the $\gamma = 1$ and $\gamma = 10$ cases.

Another test was performed to evaluate the robustness of the reconstruction algorithm to noise. Reconstructions were performed with different noise levels for both the $\gamma = 1$ and $\gamma = 10$ cases, starting from data of figures 17 and 21, respectively. The result of this procedure is shown in figure 24, where the average residuals (equation (12)) are plotted against the noise level (i.e. β of equation (10)).

As expected, the average residual follows a monotonic increasing trend with the noise level in both cases. Its value remains similar in both cases, with the $\gamma = 1$ case showing larger errors at noise levels between 10% and 30%. This is counter-intuitive, as one would expect that errors would be higher for the $\gamma = 10$ case, since it corresponds to a more complex shape. This behavior is likely attributable to the inclusion of residuals at $R \in [2.1, 2.15]$ m in the calculation defined by equation (12). In the $\gamma = 1$ case, the line of sight partially intersects the true emissivity, artificially increasing the error, whereas in the $\gamma = 10$ case, the emissivity is more localized and fully captured by the lines of sight, resulting in lower residuals. At a noise level of 40%, the maximum average residual is ≈4% for both cases, demonstrating a very high robustness to noise.

5.3. Example of energy-resolved reconstruction of a spatially localized suprathermal component

A phantom emissivity was created to test the ability of the GEM diagnostic to perform tomographic reconstructions resolved in energy. The emissivity consisted of a thermal component created in REVOLT-U using the plasma profiles of figure 7 (400 eV configuration), plus a suprathermal component created assuming Bremsstrahlung emission (equation (1)) with a fixed temperature. This value was determined by a fit to the parallel and antiparallel components of the simulated spectrum shown in figure 5(b) of [4]. To simulate a scenario in which the suprathermal component is localized in space, the Bremsstrahlung formula of the suprathermal component was multiplied by a Gaussian function of R and Z (equation (1)):

$$g(R,Z) \propto \exp\left(-\frac{(R-R_c)^2}{2\sigma_R^2} - \frac{(Z-Z_c)^2}{2\sigma_Z^2}\right) \qquad (13)$$

where $R_c = 2.1$ m, $Z_c = -0.1$ m, and $\sigma_R = \sigma_Z = 0.08$ m. The proportionality constant was determined from the simulated spectra of figure 5(d) of [4] to mimic the relative magnitude of the suprathermal component with respect to the thermal one.

At this point, it is important to emphasize that the primary goal was not to produce a high-fidelity or physically accurate emissivity model. Instead, the suprathermal component was introduced solely to evaluate the GEM diagnostic's ability to perform tomographic reconstructions across different energy bands. The emphasis was placed on demonstrating the method's functionality over a broad dynamic range, rather than on the physical realism of the emission model.

We defined the total emissivity, ϵ_{tot}, as the emissivity integrated over all energies:

$$\epsilon_{tot} = \int_E \frac{d\tilde{N}}{dE_{ph}}(E)\,dE \qquad (14)$$

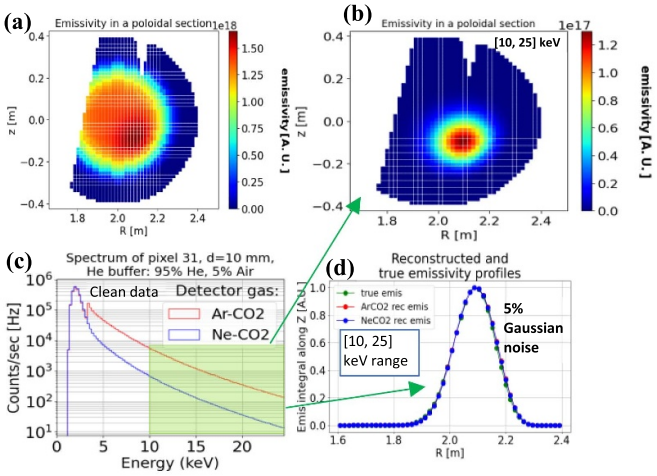

Figure 25. (a) Shows the emissivity integrated over all energies, comprehensive of both the thermal and suprathermal component. (b) Shows the emissivity integrated over the energy range [10, 25] keV, where the suprathermal component dominates the emission. (c) Shows an example of synthetic energy spectrum (clean) in a single detector pixel for two different detector gas mixtures: Ar/CO_2–70/30% and Ne/CO_2–70/30%. (d) Shows the true and the reconstructed emissivity profiles in the energy range [10, 25] keV, for both Ar/CO_2–70/30% and Ne/CO_2–70/30%. Data used for the reconstruction process were generated with 5% Gaussian noise.

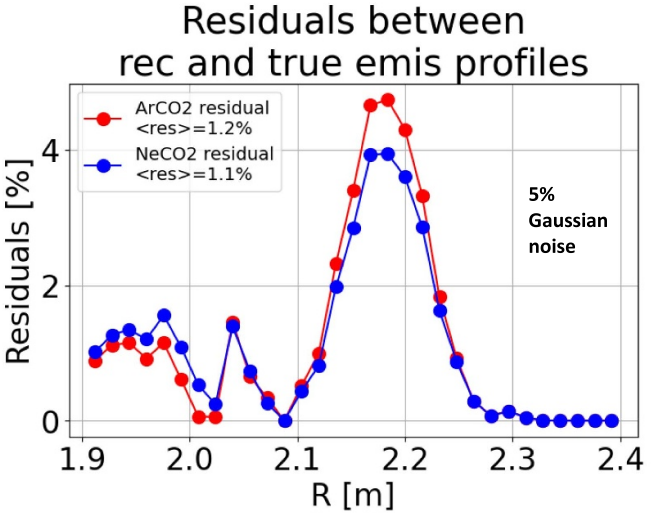

Figure 26. Residuals between the reconstructed and the true emissivity profiles of figure 25(d). Only radial positions greater than 1.9 m are shown. The average residual (calculated through equation (12)) is displayed for both gas mixtures. Reconstructions were obtained from synthetic data with 5% Gaussian noise.

where $\frac{d\tilde{N}}{dE_{ph}}(E)$ is the phantom emissivity (number of photons per unit time, volume, and energy) discussed above, comprehensive of both the thermal and suprathermal components. $\frac{d\tilde{N}}{dE_{ph}}(E)$ was used as the source emissivity in REVOLT-U, i.e. it was used to define the emissivity associated to each voxel. Then, synthetic detector data were obtained using REVOLT-U. ϵ_{tot} was not used for the calculation of synthetic detector data. Nevertheless, ϵ_{tot} is shown in figure 25(a) to illustrate how the background emissivity would obscure the true spatial structure of the suprathermal component if the tomographic reconstruction were performed by integrating counts over all energies (thus obtaining the energy-integrated emissivity). Figure 25(b) shows the integral of $\frac{d\tilde{N}}{dE_{ph}}(E)$ in the [10, 25] keV energy range. In this range, the suprathermal component dominates, effectively allowing to visualize the localization in space of the suprathermal component. This shows how equation (13) approximates the localization of a high energy electron population in space (with the aim of simulating phenomena similar to what was observed in [4]).

GEM detectors, with their energy-resolved measurements, enable the selection of photon counts corresponding to a specific energy range. In REVOLT-U simulations, this process is represented by the binning of $S(E)$. Therefore, to perform a tomographic reconstruction for each energy bin, it is sufficient to substitute S with $S(E)$ and $\mathbf{L}$ with $\boldsymbol{SF_{3D}}(E)$ in equation (8). It is worth noting that this not only accounts for geometrical factors, but also incorporates x-ray attenuation and detector efficiency, since all this information is contained in $\boldsymbol{SF_{3D}}(E)$. More often, the interest is in performing reconstructions over an energy range larger than a single energy bin. For instance, in this example, it was interesting to determine the spatial localization of the suprathermal component by performing a reconstruction in the [10, 25] keV range. The best way to proceed was by iterating the reconstructions for each energy bin in the [10, 25] keV range, rather than using detector counts directly integrated in the [10, 25] keV range. This ensured that the x-ray attenuation and the detector efficiency were properly accounted for. This procedure resulted in multiple instances of ϵ_{2D}, one for each energy bin. These were added together to obtain the fully reconstructed 2D emissivity in the [10, 25] keV energy range. Since we were using only two vertical lines of sight, the 2D emissivity was integrated along Z to obtain the *emissivity profile*.

An example of the synthetic energy spectrum (clean) in a single detector pixel is shown in figure 25(c), for two different gas mixtures: Ar/CO_2–70/30% and Ne/CO_2–70/30%. We used two different gas mixtures (Ar/CO_2–70/30% and Ne/CO_2–70/30%) to test if they were characterized by different performance. Ne/CO_2–70/30% was considered a good candidate in place of Ar/CO_2–70/30% mainly because it removes the Argon efficiency peak at 3.2 keV. However, as figure 25(c) shows, using Ar/CO_2 results in more counts at higher energies (approximately by a factor 10), reducing the statistical error on the measurements and thus making it more appealing for suprathermal tail profile reconstructions. If needed, it should be possible to change the detector gas mixture during the experimental campaign thanks to the setup discussed in section 2.

Figure 25(d) shows the true and reconstructed emissivity profiles in the [10, 25] keV range for both Ar/CO_2 and Ne/CO_2. The reconstruction was obtained through the procedure described above, using $S(E)$ with a noise level of 5%.

The residuals between the reconstructed and the true emissivity profiles for both detector gas mixtures are shown in figure 26. Residuals are shown only for $R > 1.9$ m and

the average residual (equation (12)) is displayed. The results show that Ar/CO_2 and Ne/CO_2 yield very similar performance. The slight differences can be attributed to variations in random number generation for synthetic noise and potentially to the minimization algorithm of the reconstruction process. Therefore, under experimental conditions, differences in reconstruction performance between the two gas mixtures may be primarily driven by differences in the statistical errors of the measurements, given that Ne/CO_2 is expected to lead to lower counts at high energies compared to Ar/CO_2.

6. Conclusions and future perspectives

A diagnostic design for RFX-mod2 has been proposed, including a complete CAD model of the mechanical components for the diagnostic lines of sight. Dedicated simulation tools tailored to the GEM detectors have been developed and suggest that measurements simultaneously resolved in energy, space and time should be feasible. These simulations highlighted two key requirements: (i) helium buffers to minimize x-ray attenuation between the plasma and the detectors, and (ii) a motor-driven pinhole of variable diameter for each detector to control the photon flux incident on the detectors. They have also shown that selecting Ne/CO_2–70/30 as the detector working gas is advantageous when the low-energy portion of the spectrum is of interest, because it avoids the argon absorption edge (approximately located at 3.2 keV), whereas Ar/CO_2–70/30 becomes preferable for high-energy studies due to its superior efficiency above $\sim$3 keV. Varying the helium fraction in the buffer is predicted to raise the count rate by up to four orders of magnitude as the mixture approaches pure helium. This gain, however, increases the risk of exceeding the detector's current limit or its count rate capability. To manage this risk, a scaling law has been derived to express the current as a function of the high-voltage setting and the pinhole diameter. This relation should guide the selection of operating parameters during future RFX-mod2 experiments. Before it is applied, however, its coefficients must be recalculated using a plasma emissivity model tailored to the experimental scenario of interest and calibrated against experimental data through the determination of the global fitting parameter ς (see section 3.1).

Synthetic data from simulations were employed to evaluate the feasibility of tomographic reconstruction at RFX-mod2. Given the limitation of having only two vertical view cones, a complete two-dimensional reconstruction of the plasma emissivity was not achievable with this configuration. Nevertheless, simulations indicate that it should be feasible to reconstruct emissivity profiles, even for complex plasma shapes like those expected during QSH states of RFX-mod2 plasmas. The reconstruction performance was assessed under varying noise conditions, indicating robust noise resilience of the algorithm. Specifically, the radial average residual was approximately 2% at a noise level of 10%, and approximately 4% at a noise level of 40%.

Extending the study to energy resolved reconstructions, results suggest that at least two distinct energy ranges can be independently reconstructed: one corresponding to the thermal component and another corresponding to the suprathermal component of the emission spectrum. The choice of the detector wroking gas should influence the reconstruction outcomes primarily through statistical measurement errors: using Ne/CO_2 gas should result in lower count rates (therefore greater statistical errors) at higher energies compared to Ar/CO_2.

According to simulations, in principle, arbitrary energy bands across the measured energy spectrum can be selected for tomographic inversion. Indeed, preliminary analyses (not shown in this paper) indicate that should be possible to invert specific energy bands around prominent spectral peaks, such as those resulting from x-ray-emitting impurities. However, the width of the selected bands should at least exceed the energy resolution of the detector and include sufficient statistical counts to ensure reliable reconstruction. Moreover, the accuracy of the detector calibration could also play a role in the reconstruction performance, and its influence could depend on the width of the chosen energy intervals. Future work is foreseen to investigate these aspects.

Future work will also explore inferring the electron temperature from a fit to the measured energy spectrum. For this purpose, a deconvolution algorithm to correct for detector energy resolution is under development. The impact of line-of-sight attenuation on the measured electron temperature is quantified and compensated by the algorithm.

The diagnostic commissioning will begin as soon as the detectors have been assembled and calibrated. A program of experimental tests at RFX-mod2, carried out under conservative operating conditions, will benchmark the simulations before the models are relied upon for routine operation.

Data availability statement

The data cannot be made publicly available upon publication because they are not available in a format that is sufficiently accessible or reusable by other researchers. The data that support the findings of this study are available upon reasonable request from the authors.

Acknowledgments

Project funded under the National Recovery and Resilience Plan (NRRP) in the framework of the European Union—NextGenerationEU, Mission 4, Component 2, Investment 3.1—Area ESFRI Energy—Call for tender No. 3264 of 28-12-2021 of Italian University and Research. Ministry (MUR), Project ID IR0000007, MUR Concession Decree No. 243 del 04/08/2022, CUP B53C22003070006, 'NEFERTARI—New Equipment for Fusion Experimental Research and Technological Advancements with Rfx Infrastructure'.

Author contributions

F Guiotto 0000-0001-6014-918X
Conceptualization (equal), Data curation (lead), Formal analysis (lead), Investigation (equal), Methodology (equal), Software (lead), Validation (equal), Visualization (lead), Writing – original draft (lead), Writing – review & editing (lead)

O Putignano
Conceptualization (equal), Formal analysis (equal), Investigation (equal), Methodology (equal), Software (equal), Supervision (equal), Validation (equal), Visualization (equal)

A Dal Molin 0000-0003-0471-1718
Conceptualization (equal), Investigation (equal), Supervision (equal)

G Croci 0009-0004-3302-4209
Conceptualization (equal), Funding acquisition (equal), Investigation (equal), Methodology (equal), Project administration (equal), Resources (equal), Supervision (equal), Validation (equal)

P Franz 0000-0002-4369-2348
Conceptualization (equal), Funding acquisition (equal), Investigation (equal), Methodology (equal), Project administration (equal), Resources (equal), Supervision (equal), Validation (equal)

M Zuin 0000-0002-0282-2978
Conceptualization (equal), Funding acquisition (equal), Investigation (equal), Methodology (equal), Project administration (equal), Resources (equal), Supervision (equal), Validation (equal)

L Orlandi 0009-0006-8720-5042
Resources (supporting), Software (supporting), Visualization (supporting)

A Celora 0009-0006-0160-2195
Conceptualization (supporting), Investigation (supporting), Methodology (supporting), Software (supporting)

F Caruggi 0000-0002-5480-1327
Conceptualization (supporting), Investigation (supporting), Methodology (supporting), Software (supporting)

G Grosso
Conceptualization (supporting), Funding acquisition (supporting), Investigation (supporting), Methodology (equal), Project administration (supporting), Resources (equal)

E Perelli Cippo
Funding acquisition (equal), Investigation (supporting), Project administration (supporting), Resources (equal)

M Tardocchi
Funding acquisition (equal), Investigation (supporting), Project administration (supporting), Resources (equal)

P Bettini 0000-0001-7084-4071
Funding acquisition (equal), Resources (equal)

A Muraro
Conceptualization (equal), Formal analysis (equal), Funding acquisition (equal), Investigation (equal), Methodology (equal), Project administration (equal), Resources (equal), Software (equal), Supervision (lead), Validation (equal), Visualization (equal)

References

[1] Escande D F What is a reversed field pinch? *Rotation and Momentum Transport in Magnetized Plasmas* pp 247–86
[2] Carraro L *et al* 2024 RFX-mod2 diagnostic capability enhancements for the exploration of multi-magnetic-configurations *Nucl. Fusion* **64** 076032
[3] Dexter R N, Kerst D W, Lovell T W, Prager S C and Sprott J C 1991 The Madison symmetric torus *Fusion Technol.* **19** 131–9
[4] DuBois A M, Almagri A F, Anderson J K, Den Hartog D J, Lee J D and Sarff J S 2017 Anisotropic electron tail generation during tearing mode magnetic reconnection *Phys. Rev. Lett.* **118** 075001
[5] Celora A *et al* 2024 Assessment of a space and energy resolved diagnostic based on GEM technology on MAST-U *Meas. Sci. Technol.* **36** 016019
[6] Li E, Chen Y, Qu H, Zhou T, Chen F, Zhang L, Wang H, Duan Y, Liu H and Shen B 2023 Progress of a gas-electron-multiplier based camera (GEM) in investigating EAST macroscopic instabilities *Plasma Phys. Control. Fusion* **65** 055014
[7] Franz P, Marrelli L, Murari A, Spizzo G and Martin P 2001 Soft x-ray tomographic imaging in the RFX reversed field pinch *Nucl. Fusion* **41** 695
[8] Franz P, Gobbin M, Marrelli L, Ruzzon A, Bonomo F, Fassina A, Martines E and Spizzo G 2013 Experimental investigation of electron temperature dynamics of helical states in the RFX-Mod reversed field pinch *Nucl. Fusion* **53** 053011
[9] Sauli F 2016 The gas electron multiplier (GEM): operating principles and applications *Nucl. Instrum. Methods Phys. Res. A* **805** 2–24
[10] Caruggi F *et al* 2023 Performance of a triple GEM detector equipped with Al-GEM foils for x-rays detection *Nucl. Instrum. Methods Phys. Res. A* **1047** 167855
[11] Rzadkiewicz J *et al* 2013 Design of T-GEM detectors for x-ray diagnostics on JET." *Nuclear Instruments and Methods in Physics Research Section A: Accelerators, Spectrometers, Detectors and Associated Equipment* (*Selected Papers from the 2nd International Conference Frontiers in Diagnostic Technologies (ICFDT2)*) vol 720 (Elsevier) pp 36–38
[12] Mazon D *et al* 2022 First GEM measurements at WEST and perspectives for fast electrons and heavy impurities transport studies in tokamaks *J. Instrum.* **17** C01073
[13] Pacella D, Gabellieri L, Romano A, Causa F, Murtas F, Claps G, Lee S H, Hong J, Jang J and Choe W 2013 GEM-based energy resolved x-ray tangential imaging system on KSTAR *40th EPS Conf. on Plasma Physics* vol 2 European Physical Society pp 1314–7
[14] Hu Y, Li E, Ma C and Mai C 2025 Application of a data-driven tomography method for the gas electron multiplier (GEM) based x-ray camera on EAST *Nucl. Instrum. Methods Phys. Res. A* **1073** 170281

[15] Malinowski K, Chernyshova M, Jabłoński S and Casiragi I 2021 Optimization of GEM-based detector readout electrode structure for SXR imaging of tokamak plasma *J. Instrum.* **16** C11014
[16] Chernyshova M, Dobrut M, Jabłoński S, Malinowski K and Fornal T 2022 Multi-chamber GEM-based concept of radiated power/SXR measurement system for use in high radiation environment of DEMO *J. Instrum.* **17** C05013
[17] Knoll G F 2010 *Radiation Detection and Measurement* (Wiley)
[18] Corradi G, Murtas F and Tagnani D 2007 A novel high-voltage system for a triple GEM detector *Nucl. Instrum. Methods Phys. Res. A* **572** 96–97
[19] Forster R and Godfrey T 2006 MCNP-a general Monte Carlo code for neutron and photon transport *Monte-Carlo Methods and Applications in Neutronics, Photonics and Statistical Physics: Proc. of the Joint Los Alamos National Laboratory-Commissariat À l'Energie Atomique Meeting Held at Cadarache Castle, Provence* (*22–26 April 1985*) (Springer) pp 33–55
[20] Apostolakis J, Wright D H and Collaboration G 2007 An overview of the Geant4 toolkit *AIP Conf. Proc.* **896** 1–10
[21] Guiotto F *et al* 2025 REVOLT-upgrade: a software tool for fast, energy-resolved simulations of soft x-ray detectors in nuclear fusion experiments *Meas. Sci. Technol.* **36** 075501
[22] Celora A *et al* 2024 A multipurpose numerical method for imaging studies and tomographic reconstruction *J. Instrum.* **19** C03032
[23] Guiotto F *et al* 2024 Data analysis and tomographic reconstruction via x-ray measurements with a GEM detector at the high-voltage Padova test facility *IEEE Trans. Plasma Sci.* **52** 4450–61
[24] Von Goeler S, Stodiek W, Eubank H, Fishman H, Grebenshchikov S and Hinnov E 1975 Thermal x-ray spectra and impurities in the ST tokamak *Nucl. Fusion* **15** 301
[25] Milnes J *et al* 2015 MAST upgrade—construction status *Proc. 28th Symp. Fusion Technol. SOFT-28* vol 96–97 pp 42–47
[26] Smirnov I B 2005 Modeling of ionization produced by fast charged particles in gases *Nucl. Instrum. Methods Phys. Res. A* **554** 474–93
[27] Garfield++ Collaboration Garfield++ (available at: https://garfieldpp.docs.cern.ch/) (Accessed 02 August 2025)
[28] Dassault Systèmes CATIA (available at: www.3ds.com/products/catia) (Accessed 02 August 2025)
[29] Moxtek DuraBeryllium-x-ray-Windows-WIN-DATA-1003.pdf (available at: https://moxtek.com/wp-content/uploads/pdfs/DuraBeryllium-x-ray-Windows-WIN-DATA-1003.pdf) (Accessed 02 August 2025)
[30] Standa Ltd. Motorized Iris Diaphragm model: 8MID22-0-N (available at: www.standa.lt/products/catalog/motorised_positioners?item=421&prod=motorized-iris-diaphragm) (Accessed 02 August 2025)
[31] Flicoflex FDM (available at: https://filcoflex.com/products/jacob-flexible-connections/fdm/) (Accessed 02 August 2025)
[32] Bronkhorst Reliable EL-FLOW Select mass flow meter/controller *Bronkhorst* (available at: https://www.bronkhorst.com/products/gas-flow/el-flow-select/) (Accessed 02 August 2025)
[33] MacDonald R "TN-6 diffusion rate of helium through aluminized Mylar foil", E614 experiment tech notes project mail University of Alberta 10 December 1997 (available at: https://twist.triumf.ca/private/technotes/00006/index.html) (Accessed 6 November 2025)
[34] Curioni A, Dinar N, La Torre F P, Leidner J, Murtas F, Puddu S and Silari M 2017 Measurements of ^{55}Fe activity in activated steel samples with GEMPix *Nucl. Instrum. Methods Phys. Res. A* **849** 60–71
[35] Muraro A *et al* 2019 Development and characterization of a new soft x-ray diagnostic concept for tokamaks *J. Instrum.* **14** C08012
[36] Mindur B *et al* 2016 Gas gain stabilisation in the ATLAS TRT detector *J. Instrum.* **11** 04027
[37] Alfonsi M, Bencivenni G, de Simone P, Murtas F, Poli Lener M, Bonivento W, Cardini A, Deplano C, Raspino D and Pinci D 2004 High-rate particle triggering with triple-GEM detector *Nucl. Instrum. Methods Phys. Res. A* **518** 106–12
[38] Tikhonov A N and Arsenin V Y 1977 *Solutions of ill-posed problems* (Wiley)
[39] Wingen A, Shafer M W, Unterberg E A, Hill J C and Hillis D L 2015 Regularization of soft-x-ray imaging in the DIII-D tokamak *J. Comput. Phys.* **289** 83–95
[40] Qu H, Hu L, Cordella F, Claps G, Pacella D, Xu L and Li E 2019 Application of the Tikhonov tomography method for the gas electron multiplier (GEM) system on experimental advanced superconducting tokamak *Rev. Sci. Instrum.* **90** 093507
[41] Murari A, Franz P, Marrelli L, Spizzo G, Terranova D, Zabeo L, Bilato R, Martin P, Martini S and Zanca P 1999 Tomographic imaging of RFX plasmas in various confinement regimes *26th EPS Conf. on Contr. Fusion and Plasma Physics* vol 23J (*Maastricht, 14–18 June 1999*) (*ECA*) pp 1129–32 (available at: https://info.fusion.ciemat.es/OCS/EPS1999/web/pdf/p3047.pdf)